

Leveraging Hardware Power through Optimal Pulse Profiling for Each Qubit Pair

Yuchen Zhu[†], Jinglei Cheng[‡], Boxi Li[§], Yidong Zhou[†], Yufei Ding[¶], Zhiding Liang[†]

[†] Rensselaer Polytechnic Institute, Troy, NY, USA

[‡] University of Pittsburgh, Pittsburgh, PA, USA

[§] Forschungszentrum Jülich, Jülich, Germany

[¶] University of California San Diego, San Diego, CA, USA

(liangz9@rpi.edu)

Abstract—In the scaling development of quantum computers, the calibration process emerges as a critical challenge. Existing calibration methods, utilizing the same pulse waveform for two-qubit gates across the device, overlook hardware differences among physical qubits and lack efficient parallel calibration. In this paper, we enlarge the pulse candidates for two-qubit gates to three pulse waveforms, and introduce a fine-grained calibration protocol. In the calibration protocol, three policies are proposed to profile each qubit pair with its optimal pulse waveform. Afterwards, calibration subgraphs are introduced to enable parallel calibration through identifying compatible calibration operations. The protocol is validated on real machine with up to 127 qubits. Real-machine experiments demonstrates a minimum gate error of 0.001 with a median error of 0.006 which is $1.84 \times$ reduction compared to default pulse waveform provided by IBM. On device level, a double fold increase in quantum volume as well as $2.3 \times$ reduction in error per layered gate are achieved. The proposed protocol leverages the potential current hardware and could server as an important step toward fault-tolerant quantum computing.

I. INTRODUCTION

Recent advances in quantum computing have demonstrated impressive scaling in qubit numbers, with leading platforms now reaching hundreds of physical qubits [1], [9]. However, achieving high-fidelity quantum operations on these large-scale systems remains a critical challenge [55], [3], [47], [10]. While single-qubit gate fidelities often exceed 99.9% [14], [5], two-qubit gate fidelities on multi-qubit, fixed-frequency superconducting chips typically lie around 99% [13], [50], significantly higher than the 0.1% error rates on specialized two-qubit devices. As one of the leading quantum computing platforms, superconducting quantum systems also face challenges in maintaining high-fidelity operations as the system scales up, which signifies the importance of a good calibration protocol.

Superconducting quantum computers operate at extremely low temperatures in high-vacuum environments to maintain quantum coherence [22]. These systems rely on microwave pulse control for qubit manipulation and measurements. The microwave signals define the system Hamiltonian and the qubit evolution, while the reflected signals of measurement pulses enable quantum state measurements. The quality of quantum operations depends on the precise calibration of these control systems [6], [17]. Precise control involves two key aspects:

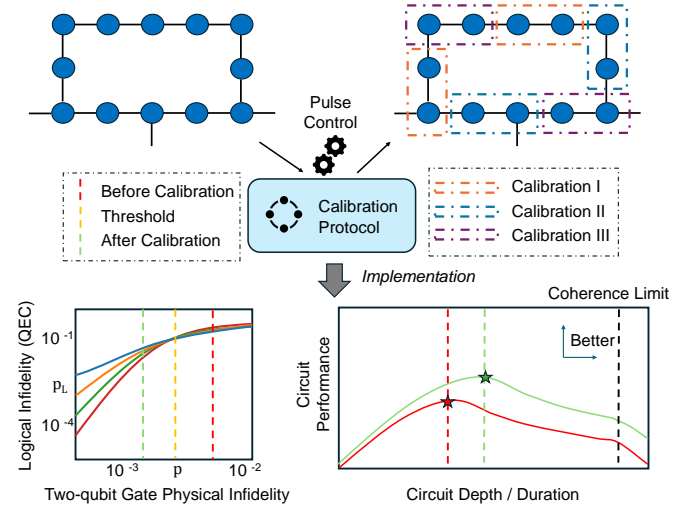


Fig. 1: Overview of the proposed hardware-aware calibration protocol and its impact.

generating accurate microwave pulses and performing regular calibrations to compensate for system drift and external perturbations. The control parameters include pulse amplitudes, frequencies, and durations, which must be carefully calibrated based on measurements of current qubit properties [20], [12], [49]. To maintain optimal operation conditions and keep error rates within acceptable ranges, quantum hardware providers like IBM perform calibration routines at both hourly and daily intervals [38]. Regular calibration ensures that qubits perform the designed operations. While individual gate errors may appear insignificant in isolation, their cumulative effect becomes significant as circuit depth increases and the number of gates grows. As these errors accumulate, they can significantly degrade the overall fidelity of the quantum circuit, and eventually make the execution of quantum algorithms unreliable [21], [52], [39], [53], [15].

Calibration is also critical for Quantum Error Correction (QEC) since when effective calibration is applied to reduce the physical error rates below a critical threshold, QEC can exponentially suppress logical errors by increasing the code distance [7], [42]. Recent advancements, such as below-threshold operation of surface codes [35] and hardware-

efficient schemes like bosonic cat qubits [54], have shed light on the potential of QEC in the near future. These advances have driven extensive experimental efforts to optimize QEC protocols in real quantum systems. Related works [4], [23], [40], [33] demonstrate that achieving high-fidelity operations for practical QEC demands precise calibration. However, traditional calibration methods face significant challenges. First, they often ignore differences in qubits’ properties. Second, the extended duration of calibration—spanning hours or days [38]—introduces system drift that affects the system performance. Finally, existing approaches emphasize a trade-off between calibration time and fidelity but neglect hardware-specific optimizations and the strict timing requirements of QEC protocols. These limitations are particularly severe in calibrating cross-resonance (CR) gates which are essential for two-qubit operations in modern quantum processors. As QEC becomes a cornerstone of fault-tolerant quantum computing, it imposes rigorous demands on gate fidelities and control accuracies.

A key challenge in CR gates arises from unwanted excitations of the control qubit due to off-resonant drives. The standard derivative removal by adiabatic gate (DRAG) technique addresses this issue for single transitions [32], [11], but quantum systems often exhibit multiple transition pathways that need simultaneous control. Multi-derivative DRAG offers a solution by applying recursive corrections to suppress multiple transitions simultaneously [24]. This method adds derivative terms to the control pulse that target specific energy transitions between quantum states. While this approach can enhance gate fidelity, its effectiveness depends on system parameters such as the frequency difference between qubits. These implementation considerations motivate the need for a systematic approach to optimize calibration across multiple qubit pairs simultaneously.

To optimize the calibration process across qubit pairs, we introduce a novel calibration protocol with three different calibration policies: **(1) Brute-force Clustering**, where qubit pairs are grouped based on key physical properties, representative pairs are selected for calibration, and the optimized Echoed Cross-Resonance (ECR) gates’ waveforms are generalized; **(2) Topology-oriented Representative**, which leverages the regular patterns in heavy-hex lattice topologies by classifying qubit pairs according to their positions within unit cells, calibrates representatives for each position, and generalizes the optimized waveforms; and **(3) Hardware-oriented Policy**, which incorporates system knowledge and hardware limitations, such as frequency detuning relationships and decoherence times, to select the most efficient and practical waveform strategies for each qubit pair.

Our policies also offers a practical balance between calibration accuracy and computational efficiency, which is particularly important for scaling up quantum processors. However, successful local optimization of qubit pairs is only the first step toward processor-wide calibration. We address processor-wide calibration by treating the quantum processor as an undirected graph G , where nodes represent qubits and edges represent

coupled qubit pairs. To minimize calibration time, we develop a parallel calibration protocol that partitions the coupling graph into calibration subgraphs. Each subgraph consists of edges that can be calibrated simultaneously without mutual interference, achieved by maintaining a minimum distance of two between concurrent calibrations. This parallelization strategy significantly accelerates the calibration process while preserving calibration accuracy. For instance, in a 127-qubit heavy-hex architecture, our approach enables simultaneous calibration of up to 38 qubit pairs distributed across five subgraphs, substantially reducing the total calibration time compared to sequential methods.

We illustrate the brief overview of our protocol in Figure 1. Our protocol optimizes calibration policies and assigns different pulse envelopes to qubit pairs as the colored blocks in the top-right of Figure 1. The bottom-left of Figure 1 shows the effectiveness of quantum error correction at various code distances, represented by different colored curves. Our protocol achieves two key improvements: it reduces two-qubit gate physical error rates below the error correction threshold, enabling effective quantum error correction and significantly improving logical error rates; and it optimizes system performance by reducing calibration overhead, shortening circuit duration, and enhancing overall circuit fidelity compared to conventional calibration approaches, as shown in the bottom-right of Figure 1.

In this work, we introduce a novel fine-grained calibration protocol with three major contributions:

- A novel calibration protocol with multiple components: 1) Three calibration policies to assign waveform candidate to qubit pairs according to their profiling results. 2) A graph-based parallelization algorithm for scaling up the protocol that performs the calibration simultaneously.
- The first large-scale implementation of multi-derivative DRAG and direct CR operations on real quantum machines, which advances quantum control techniques in practice.
- Extensive experimental results with up to 127 qubits that show a $1.84\times$ reduction in terms of the medium of the two-qubit gate error rate, $1.26\times$ reduction in pulse duration, up to $25\times$ reduction in calibration overhead, double of the quantum volume, and up to $2.3\times$ reduction in error per layered gate.

II. BACKGROUND

A. Calibration and Characterization in Quantum Gates

In quantum computing, qubits and quantum gates exhibit extreme sensitivity to external disturbances [37]. Calibration and characterization thus serve as essential procedures in quantum hardware experiments. For superconducting qubits, quantum gates operate through precise control pulses, which require careful tuning of multiple parameters: drive frequency, amplitude, phase, and duration [25]. Each parameter affects the qubit’s dynamics directly. For example, small amplitude deviations can cause over-rotations or under-rotations of qubits.

These errors accumulate and degrade overall circuit performance and fidelity as operations scale. Therefore, amplitude adjustments must be performed through iterative, fine-grained calibration routines. This process requires amplitude tuning in small increments to achieve the desired qubit state transition, which aligns actual gate behavior more closely with the intended ideal operation. Moreover, these parameters need continuous optimization to maintain stability over time, particularly in the presence of inherent hardware variations such as frequency drifts and crosstalk. To optimize the calibration of qubits, we need to understand the properties of quantum gates on the qubits. Characterization techniques reveal crucial insights into the performance of quantum gates in physical devices [36]. Quantum Process Tomography (QPT) is an approach that constructs the entire quantum process matrix for a certain quantum gate [30]. This method requires qubit preparation in various input states, gate application, and measurement of output states to characterize the gate’s behavior fully. However, QPT’s bad scalability and it’s not applicable to larger systems. Randomized Benchmarking (RB) [19] presents a more efficient alternative for characterization. This statistical approach determines average gate error rates through random gate sequences applied to qubits. Modern implementations often incorporate interleaved randomized benchmarking [28], where a specific gate of interest alternates with random Clifford operations, enabling characterization of individual gate performance within the broader context of circuit operation.

B. Echoed CR

The Echoed Cross Resonance (Echoed CR) pulse [2] is an existing implementation method for two-qubit gates in superconducting quantum computing, particularly for the CNOT gate implementation. The standard CR pulse has multiple Hamiltonian terms: ZX, ZZ, ZI, IX, IY , and others. The Echoed CR pulse is built upon the CR pulse by adding an “echo” mechanism to reduce phase errors and unwanted couplings during gate operation. This echoing procedure eliminates unwanted Hamiltonian terms and preserves the desired ZX interaction. The result implements an effective gate operation of $\frac{1}{\sqrt{2}}(IX - XY)$. Therefore, to calibrate the Echoed CR pulse, we need to calibrate the CR pulse within it. Unwanted ZZ interaction that causes phase errors can be addressed by ZY DRAG calibration [29]. This technique modifies the control pulse through a standard Gaussian pulse with an additional Gaussian derivative component and lifting. The calibration process focuses on the selective cancellation of remaining ZY, IX, IY terms through iterative adjustments of CR and target qubit drive pulses. The system performs two tomography experiments per calibration round to refine the pulse parameters. Hamiltonian tomography [41] is adopted to measure the target qubit’s response with various time intervals. The data from Hamiltonian tomography enables the decomposition of the Hamiltonian into Pauli terms:

$$\hat{H}(\Omega_{\text{CR}}, \Omega_{\text{T}}) = \nu_{ZX} \hat{Z} \hat{X} + \nu_{ZY} \hat{Z} \hat{Y} + \nu_{IX} \hat{I} \hat{X} + \nu_{IY} \hat{I} \hat{Y} + \nu_{ZI} \hat{Z} \hat{I}. \quad (1)$$

The suppression of ZZ effects requires precise IY DRAG calibration. This process involves sampling three different IY DRAG amplitudes to identify zero points of the ZZ coupling strength through linear fitting. The measured IY coefficient represents the detuning strength between drives. Proper calibration of the IY DRAG reduces ZZ coupling, which would otherwise affect CR pulse fidelity. The final implementation uses an echoed pulse sequence. This sequence consists of a primary CR pulse followed by a reversed CR pulse. For an echoed CNOT gate, each CR pulse must last one-eighth of the period, as the target qubit rotates in opposite directions based on the control qubit state. This precise timing ensures accurate 90-degree ZX rotation.

C. Direct CR

Direct CR [8] is more expensive in terms of calibration cost against Echoed CR because of it based on Echoed CR with additional technologies involved.

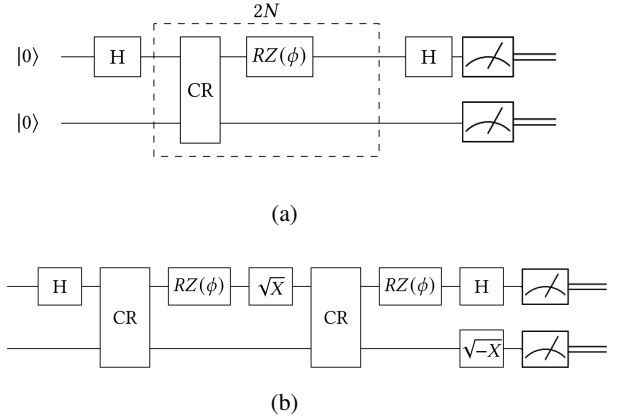


Fig. 2: (a) Calibration circuit for Z phase for the direct CR. (b) Verification circuit for the direct CR.

The calibration process begins with adjustment on target qubit signals to satisfy the condition $\nu_{IX} = \nu_{ZX}$. This adjustment ensures the target qubit rotates only when the control qubit exists in the $|1\rangle$ state. The adjustment is implemented through the iterative calibration process described in the echoed CR calibration. The next phase addresses the problem of phase shift on control qubit, which is introduced by the Stark effect with the CR pulse. This calibration step is the key difference from echoed CR calibration. In summary, the Echoed CR pulse automatically cancels phase shifts, but direct CR requires specific phase calibration. The phase calibration process employs two specific circuit configurations, as shown in Figure 2a and 2b. The circuit in Figure 2a implements a sequence of $2N$ uncalibrated CR pulses, each paired with an $RZ(\phi)$ rotation on the control qubit. Hadamard gates bracket this sequence to measure the accumulated phase shifts. The circuit returns to its initial state only when the CR pulses combined with the rotation produce a standard CNOT with a 0-degree or 180-degree phase shift. Figure 2b presents

a verification circuit that confirms the implementation of a proper CNOT gate.

III. MOTIVATION

Existing calibration methods face two major challenges: hardware inconsistencies and high calibration costs. While recent advancements propose solutions through noise-aware optimization, adaptive protocols, and real-time feedback, these approaches often introduce significant overhead in both computation and time resources. This overhead can substantially reduce quantum processor availability for practical workloads. Therefore, an improved calibration protocol must achieve three key objectives: (1) address hardware-specific variations, (2) maintain high fidelity with reasonable latency, and (3) minimize calibration costs while ensuring system performance.

A. Hardware Variability in Superconducting Quantum Systems

Hardware limitations fundamentally restrict the performance of superconducting quantum computers. These constraints result in weak qubit interaction strength and low quantum gate fidelity, which make precise calibration technology essential for reliable operation. The significant differences in relaxation time (T_1) and dephasing time (T_2) between qubit pairs create a critical challenge. Short decoherence times lead to rapid quantum information loss in qubits, which directly affects the fidelity of two-qubit operations. This inconsistency requires individual calibration protocols for each qubit pair and adds substantial complexity to system maintenance. Furthermore, fabrication variations and material differences cause wide frequency detuning values across qubit pairs. These inherent hardware variations mean that standardized calibration methods and uniform control pulses **cannot** achieve optimal performance across all qubit pairs, which results in reduced overall gate fidelity. This hardware-specific behavior demands more sophisticated, tailored calibration approaches. We address this problem in Section IV-B.

B. Missing Performance Metrics in Traditional Calibration

Traditional calibration methods rely on single-gate fidelity as the primary performance metric, which provides an incomplete picture of quantum **system** performance. Advanced compilation techniques [46], [48], [45], [26] have revealed that optimizing individual gate fidelity alone fails to capture critical system-level effects, such as qubit idle times and decoherence during circuit execution. Quantum Volume addresses these limitations by providing a metric that includes both qubit quality and system performance. However, current calibration techniques continue to focus on optimizing isolated metrics like gate fidelity or latency, without incorporating metrics like Quantum Volume. This narrow focus on performance assessment leads to suboptimal calibration strategies that fail to capture the true capabilities of quantum devices. We demonstrate gate-level, calibration-level, device-level and application-level improvements of our protocol in the Section V.

C. High-overhead and Infrequent Calibration

Current generalized calibration approaches face significant limitations due to the high costs associated with the calibration process. These costs lead to infrequent calibration, which allows system drift and errors to accumulate over time. The problem is especially severe for two-qubit gates, which are essential for advanced quantum algorithms and error correction but require longer calibration times to maintain coherence. There is an inherent trade-off between more frequent calibration to improve gate fidelity and the system downtime this calibration requires. On IBM quantum hardware, two-qubit gates need long calibration cycles to reach acceptable fidelity levels, and this results in extended downtimes. During these periods, system properties can drift, and this causes unexpected errors even in simpler single-qubit gates. Current calibration approaches do not perform calibration often enough to sufficiently mitigate these issues.

Experiments on IBM hardware demonstrate the consequences of insufficient calibration. Measurements showed error rates for single-qubit gates that reached as high as 10^{-2} when trying to excite qubits to the $|1\rangle$ state. These high error rates highlight the impact of infrequent calibration on gate fidelity. As circuits grow in size, errors from two-qubit gates and drifting system properties accumulate, and this significantly affects the computational results. IBM's current calibration standards focus on weekly full calibration of only a limited number of qubit pairs. Daily measurements include phase calibrations for just a few pairs. This approach allows substantial system drift to occur, as the minor fidelity improvements from more frequent calibration are considered unjustified given the high calibration costs. This significantly limits gate fidelity and computational accuracy, especially as quantum circuits become larger. We address the challenge of large-overhead calibration by parallel calibration as described in Section IV-C.

IV. PROTOCOL

In this section, we are introducing our proposed calibration protocol. The performance of current quantum hardware is leveraged and characterized through 4 steps, as depicted in Figure 3.

Enlargement of candidate waveform. Three distinct waveforms are developed, each capable of implementing the same basis two-qubit gate on current quantum hardware. These waveforms offer trade-offs among gate fidelity, calibration cost, and gate duration, providing flexibility in optimizing quantum operations based on system constraints.

Optimal pulse profiling. In this step, multiple policies are employed, aiming at profiling each qubit pair with its own optimal pulse waveform. The policies are designed upon the physical properties, topology similarity and system knowledge.

Parallel Calibration. After the optimal pulse is decided, a parallel graph traversal is implemented to calibrate all qubit pairs with limited time.

Benchmarking. The improvement brought about by optimal

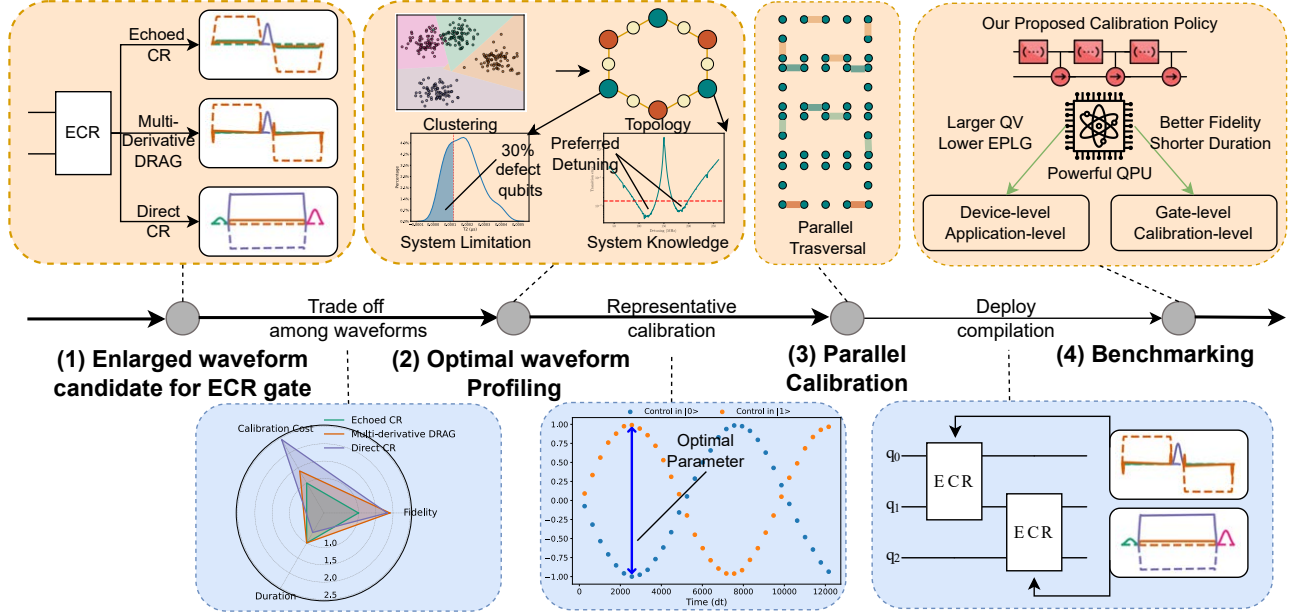


Fig. 3: Overview of the proposed calibration protocol design. With enlarged pulse candidates for ECR gate, optimal waveform profiling is achieved by the proposed calibration policies. Parallel calibration is adopted to accelerate the calibration process. The effectiveness of the protocol is examined from gate-level, calibration-level, device-level, and application-level.

pulse profiling is characterized from gate-level, calibration-level, device-level, and application-level.

A. Multi-derivative Drag

Ideally, the CR interaction leads to a rotation in the target qubit status and leaves the control qubit unaltered. However, the off-resonant microwave drive may excite the control qubits during the operation, especially when the frequency detuning between the qubits is smaller than their anharmonicities. To overcome the unwanted excitations, a term proportional to the derivative of the drive pulse is introduced, the DRAG pulse, given by $\Omega - ia \frac{\dot{\Omega}}{\Delta}$.

For the off-resonant CR drive, all the transitions among the three states ($|0\rangle$, $|1\rangle$ and $|2\rangle$) of the control transmon need to be avoided simultaneously. Therefore, multi-derivative DRAG was applied to suppress the undesired transitions by recursively applying the DRAG correction targeting three dominant transitions [24], [31]

$$\Omega_{\text{CR}}^{\text{P}} = \mathcal{F}_{\Delta_{21}}^{(1)} \circ \mathcal{F}_{\Delta_{10}}^{(1)} \circ \mathcal{F}_{\Delta_{20}}^{(2)}(\Omega) \quad (2)$$

where $\Omega = \mathcal{F}_{\Delta}^{(n)}(\tilde{\Omega}) := \left(\tilde{\Omega}^n - i \frac{d\tilde{\Omega}^n}{dt} \frac{1}{\Delta} \right)^{\frac{1}{n}}$ and Δ_{jk} denotes the energy difference between state $|j\rangle$ and $|k\rangle$. The circle operator applies the pulse shape transformation \mathcal{F} on top of the last pulse output. The initial input pulse shape needs to be chosen so that the final pulse shape still starts and ends at zero [24].

Another major portion of the CR error derivatives from other dynamical operators in the two-qubit subspace that do not commute with the ideal dynamics ZX. For instance, the

unwanted terms in Equation 1 can be measured by Hamiltonian tomography and calibrated away, as in the standard CR pulse [41]. The remaining terms, such as the ZZ and IZ error [27], are also removed by DRAG corrections on the target qubit and adjusting the detuning [24].

Despite the improvement in gate quality, the multi-derivative pulse introduces additional calibration overhead. The calibration of the DRAG correction requires more tomography experiments and hence longer calibration time. The waveform generated under the multi-derivative DRAG tends to be more complicated, therefore challenging the hardware configuration and resource optimization for current quantum hardware. During calibration experiments on real quantum hardware, a preprocessing error is sometimes detected due to the overwhelmingly complicated waveform. More importantly, through numerical simulations, previous work has proved that multi-derivative DRAG waveform achieves the most significant improvement in a certain range of qubit-qubit detuning, e.g. as shown in Figure 6. Consequently, applying multi-derivative DRAG may be unnecessary for qubits with frequency detunings outside of this interval.

B. Calibration Policy Design

The proposed approach involves three pulse waveforms, and a straightforward solution would be to conduct calibration for all three waveforms across every qubit pair. However, this method would be resource-intensive and time-consuming. Due to hardware limitations and external disturbances, modern quantum hardware experiences considerable error drift; specifically, qubit pairs typically reach an error level $5\times$ their initial

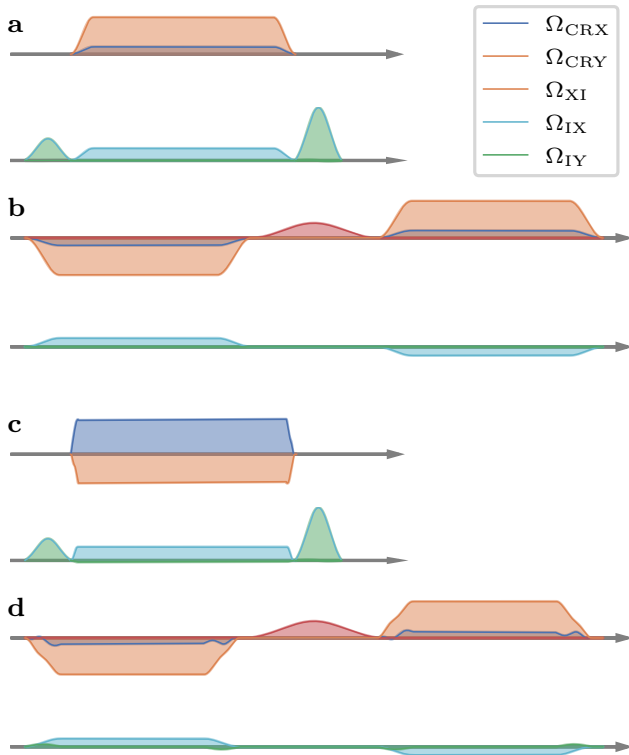


Fig. 4: Examples of the CR pulse: the default pulse shape for direct (a) and echoed (b) CR as well as the multi-derivative direct CR (c) and echoed (d). The pulse amplitudes are rescaled for visualization purposes.

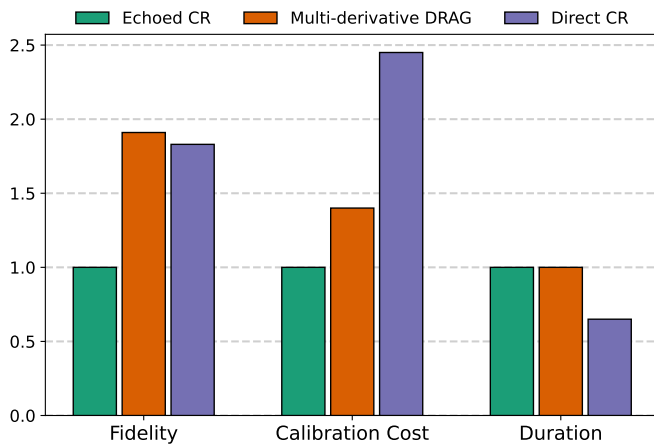


Fig. 5: Fidelity, calibration cost, and duration trade-off among various ECR gate waveforms.

value within approximately **20 hours**. To maximize fidelity while minimizing calibration time, an efficient policy should be developed to identify and calibrate the optimal waveform for each qubit pair.

1) *Waveform Candidates and Analysis*: Based on previous discussions, any ECR gate could have multiple implementa-

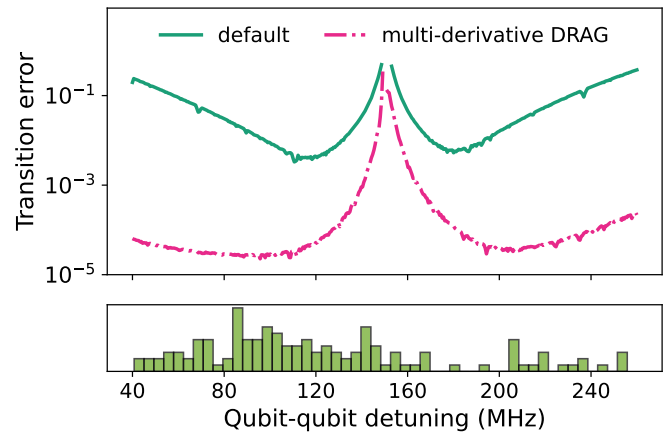


Fig. 6: Top: Relationship between remaining transition errors and the frequency detuning for multi-derivative DRAG pulse. The large error in the middle is located at half of the control qubit’s anharmonicity, induced by a two-photon transition. Bottom: Distribution of the qubit-qubit detuning on ibm_brisbane. A few outliers are removed for clarity.

tions, including the echoed CR waveform, the Multi-derivative DRAG waveform, and also the Direct CR waveform. Though the Direct CR waveform is calibrated towards the goal of realizing a CX operation, it could also be utilized to implement an ECR gates’ waveform with an SX waveform and an X waveform on the target qubit. The cross-resonance part in the Direct CR can also be designed as containing multi-derivative parts. Therefore, the waveform candidates to realize an ECR gate are enlarged to four, as shown in Figure 4. However, calibrating the original direct CR waveform on real quantum hardware has been found to be exceedingly resource-intensive. As a result, in the following discussions, the Direct CR is implemented with multi-derivative parts.

Though various waveforms can be utilized to realize the same gate, a trade-off between gate fidelity, calibration cost, and duration exists among various waveforms. Multi-derivative DRAG and Direct-CR waveforms share a potential to achieve a higher fidelity than the echoed CR, while the prior introduces a 1.4 times increase in calibration cost, and the latter one requires a calibration cost as high as 2.8 times (Figure 5). However, the short duration of the Direct CR waveform is particularly critical for qubits with limited decoherence times, as it helps mitigate coherence loss during operations. Therefore, an important problem exists as profiling each qubit pair with its own optimal pulse waveform.

2) *Brute-force Clustering*.: CR pulses use microwave to trigger Rabi oscillation on the target qubits depending on the state of the control qubit. However, the effect of Rabi oscillation and corresponding errors depend heavily on the physical properties between qubits. For example, a strong drive signal can often lead to coherent errors induced by non-adiabatic dynamics. To capture the interactive Hamiltonian between adjacent qubits, several critical metrics are consid-

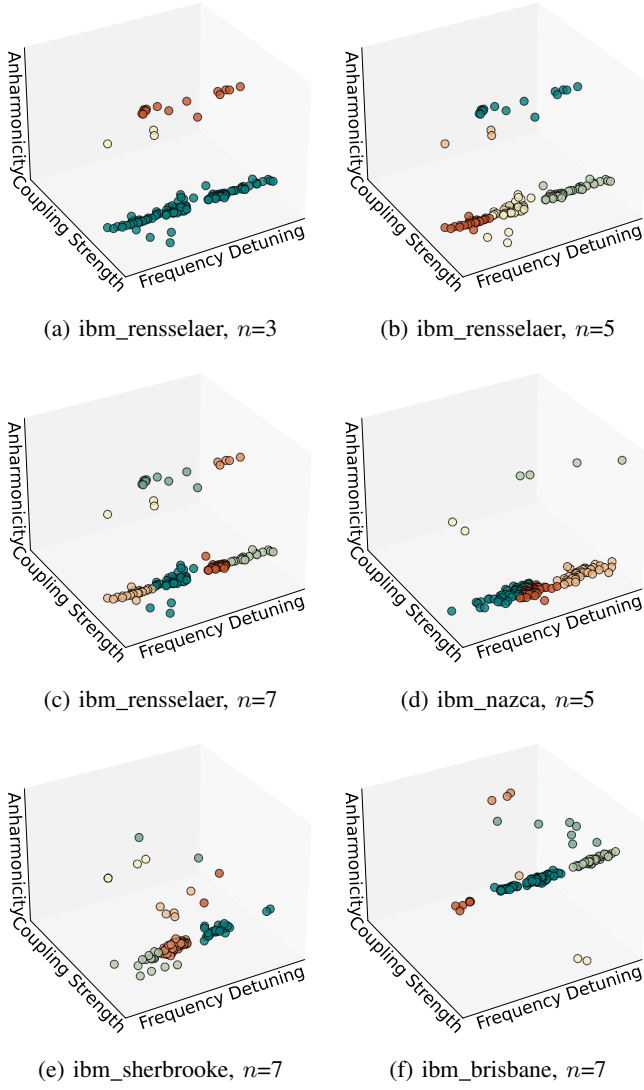


Fig. 7: Clustering results for various quantum devices (ibm_renselaer, ibm_nazca, ibm_sherbrooke, and ibm_brisbane) based on frequency detuning, coupling strength, and anharmonicity for various clustering size n .

ered, including the detuning between qubits' frequency, the anharmonicity, and the coupling strength between the qubits. As shown in Figure 6, the transition errors on the control qubit depend strongly on the qubits detuning and the anharmonicity. Apart from the control qubit error, the dominant coefficients in the effective Hamiltonian in Equation 1 are also decided by the frequency detuning and coupling strengths, given by

$$H_{CR} = -\frac{\Delta_{12}}{2}\hat{Z}\hat{I} + \frac{\Omega(t)}{2}(\hat{I}\hat{X} - \frac{J}{2\Delta_{12}}\hat{Z}\hat{X}) \quad (3)$$

where Δ_{12} is the frequency detuning between two qubits and $\Omega(t)$ is the cross resonance drive strength.

The frequency detuning, coupling strength, and anharmonicity of target qubits are prioritized as major features when profiling the optimal CR pulse. Each qubit pair is projected

into a multi-dimensional vector, which captures the physical properties that are critical to high-fidelity control. Those vectors are clustered with the Birch algorithm into multiple groups, and partition qubit pairs into sets with similar characteristics. Then one representative qubit pair is selected from each group and three calibration processes are performed on the representatives. The election of the representative allows us to identify the control waveform with optimal fidelity that can be generalized to all pairs within the cluster. To balance calibration efficiency and fidelity, the cluster size is selected to be three, five, and seven. We note that fewer groups result in a faster calibration process, and more groups would lead to a higher accuracy. We implement this approach on multiple real quantum devices, the results are illustrated in Figure 7. The clustering-based approach optimally distributes calibration resources ensures an effective trade-off between computational efficiency and calibration accuracy across qubit pairs.

3) *Topology-oriented Representative*: The Brute-force clustering method manages to strike a balance between calibration cost and the accuracy for waveform profiling. However, the performance of Brute-force clustering depends heavily on the clustering size, which is a hyperparameter predefined, and it is uncertain how many clusters are required to meet the sweet spot of the method for various quantum computer systems.

Recently, the topology of all active IBM quantum devices is based on the heavy-hex lattice, where each unit cell of lattice consists of a hexagonal arrangement of qubits, with an additional qubit on each edge. For CR operations, the resonance frequency executed on the target qubit needs to be precisely off-resonant with neighboring qubit transition frequencies to prevent unwanted interactions, also known as frequency collisions. Compared with the traditional square lattice model, the reduced connectivity of heavy-hex topology brings about fewer frequency constraints, providing a better chance at achieving higher fidelity CR control gates. Previous research has highlighted a recurring pattern among unit cells in the heavy-hex lattice topology [43], [34], where qubits occupying analogous positions across different unit cells exhibit similar physical characteristics. This regularity is a result of the uniform structure of the heavy-hex architecture, where each unit cell maintains a consistent arrangement, leading to shared properties such as frequency detuning, coupling strength, and anharmonicity among qubits in equivalent positions. Figure 8 depicts such a similarity where colors indicate the pattern of distinct frequencies for control and target. Leveraging this structural regularity, each edge in the heavy-hex topology can be classified according to its relative position within the unit cell. By categorizing edges in this way, the calibration complexity is effectively reduced. For each distinct position within the local unit cell, we select a representative edge to undergo the complete three-stage calibration process. This allows us to identify the waveform that achieves optimal fidelity, which can then be generalized to all edges in equivalent positions across the lattice. This approach significantly streamlines the calibration process by minimizing redundant calibrations, making it possible to apply a high-fidelity waveform to all similar

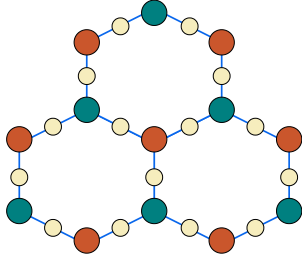
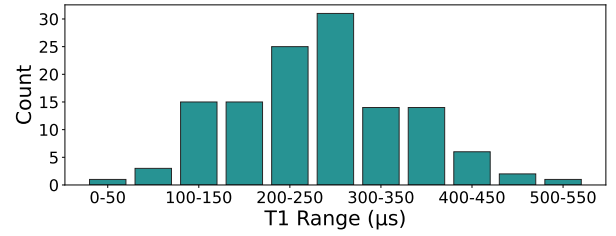


Fig. 8: Repetitive pattern of the heavy-hex lattice, colors indicate the pattern of distinct frequencies for control qubits (pale yellow) and two sets of qubits (orange and deep teal).

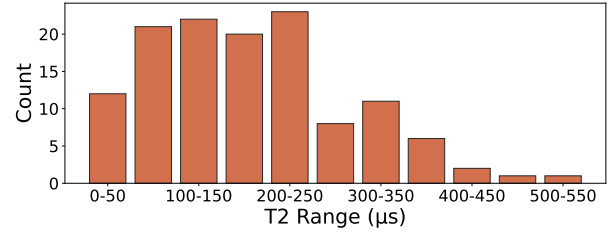
edges with greater efficiency. Compared with the Brute-force clustering, such a method limits the cluster size to 12 and the classification policy not only includes evident qubit physical parameters but also considers the hidden constraints generated by hardware topology.

4) *Hardware-oriented Policy*: Previous solutions have generated waveform profiling for all qubit pairs towards the highest fidelity while limiting a reasonable calibration time. Another critical factor, system knowledge, has been underscored by previous research as essential for optimizing performance on real quantum hardware [18], though it was not addressed in previous discussions. Typical elements of system knowledge encompass the sequential order of calibrations required to initialize and optimize a qubit, as well as targeted optimizations tailored to specific qubit pairs. The calibration sequence involves channel frequency calibrations and single-qubit calibrations, which are out of the scope of this paper. On the other hand, targeted optimizations could contribute majorly to a more efficient and accurate waveform design. In the hardware-oriented policy, system knowledge of the relationship between frequency detuning and waveform is selected as a major constraint when profiling pulse waveforms. Through numerical simulations, it's exploited that for qubit pairs that reside outside a specific frequency range, calibrating multi-derivative waveform takes much longer time than echoed CR pulse and fails to eliminate error terms to an ideal extent (0.015MHz). Therefore, for such qubit pairs, the echoed CR waveform should be directly adopted to increase the efficiency of the calibration process and improve the calibration accuracy.

Another crucial metric that is missed from previous discussions is the decoherence limit of current quantum computer systems, which exists as an important limit for the duration of quantum programs. The decoherence limit includes the longitudinal relaxation (T1) and the transverse relaxation (T2), which describes how long the excited state and the superposition state of the qubits can be preserved, respectively. As we can observe from Figure 9, for current quantum hardware, the median of T1 and T2 are $269 \mu s$ and $172 \mu s$, respectively. A typical pulse of ECR gate takes approximately 665 ns to execute. For an average-quality qubit pair, this implies that the theoretical upper bound on the number of sequential



(a) T1 distribution for ibm_renselaer



(b) T2 distribution for ibm_renselaer

Fig. 9: Longitudinal relaxation (T1) and transverse relaxation (T2) time distribution for ibm_renselaer, indicating a non-negligible number of qubit pairs with T1 or T2 below $150 \mu s$.

ECR gates that could produce meaningful results is about 258. However, the actual scenario is more severe as the general performance of a quantum program is limited by qubit pairs with the worst performance. For contemporary hardware systems with 127 qubits, the minimal T2 could be only $20 \mu s$, and around 20 qubit pairs bear a decoherence limit of less than $60 \mu s$. For those qubit pairs, the effectiveness of various waveform strategies is constrained not only by the achievable fidelity but also by the duration of the pulses. Specifically, while an echoed CR pulse may achieve the highest fidelity, its longer duration often renders it less practical than a direct CR pulse. The latter, typically requiring around 60% to 80% the duration of the former, tends to be the preferred choice in scenarios where minimizing pulse duration is critical to overall performance.

C. Graph traverse and parallelization

After individually profiling each qubit pair with its optimal CR pulse waveform, a significant challenge remains: calibrating all qubit pairs within a specific time frame without stalling the quantum machine for too much time. A coupling graph with N nodes and E edges is seen as an undirected graph G . The scheduling problem could be redefined as learning the optimal pulse parameter for some subset of edges in the coupling graph while limiting unwanted interactions outside the subset, which is referred to as $G^* \in G$. Calibration is accomplished by traversing G while calibrating parameters associated with each edge in the target G^* as shown in Figure 10.

As provided in Figure 11, the spacetime structure of the calibration process is defined as calibration subgraphs. Each subgraph represents the part of the graph which is simultaneously calibrated. The separation of calibration subgraphs

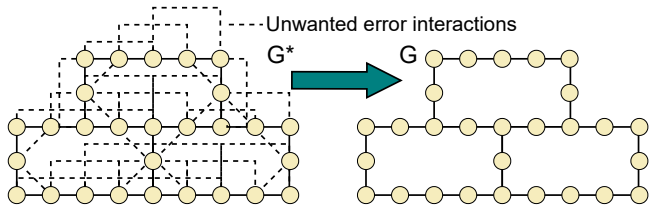


Fig. 10: Calibration target: remove unwanted interactions from a connected graph to reach its subgraph, where all edges are calibrated with optimal parameters.

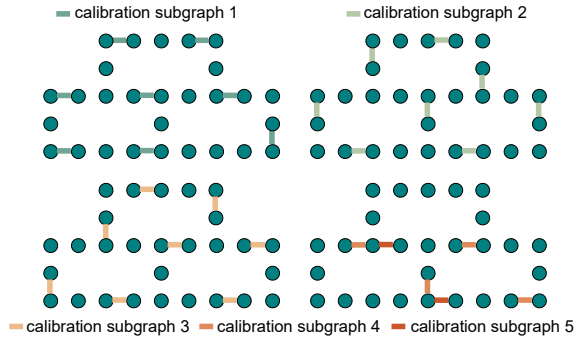


Fig. 11: Dividing a heavy-hex coupling graph into five calibration subgraphs for parallel graph traversal.

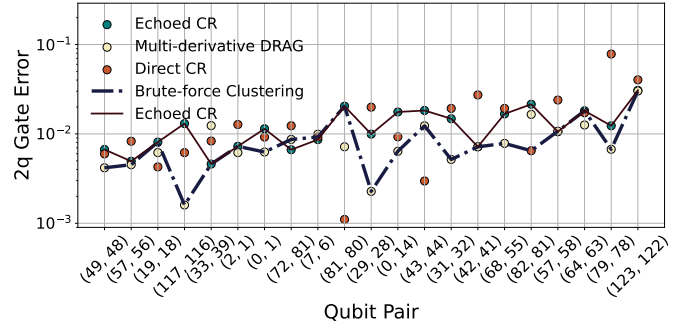
depends on the elements that could interfere with each during the calibration process. When calibrating CR pulses, it can be seen as executing ECR gates. Therefore, the calibration subgraph could be decided as the maximum number of ECR gates that could execute at the same circuit layer. In general, the total graph G is traversed after the calibration, and at each step, all edges at the subgraph are calibrated. To build the calibration subgraphs, all single paths with a length of one are selected from the coupling map. Then they are separated with the requirement of a minimum distance of two for all edges in a single calibration subgraph. For the heavy-hex structure with 127 qubits, the number of the calibration subgraph could be limited to five, with a maximum number of 38 qubit pairs calibrating simultaneously.

V. EVALUATION

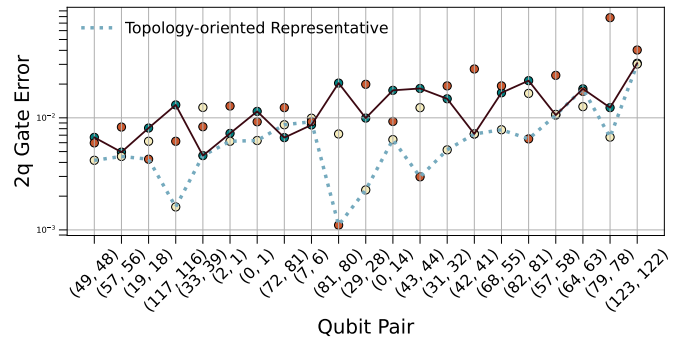
A. Configuration

All experiments are conducted on Eagle r3 quantum processors provided by IBM quantum service, including `ibm_renselaer`, `ibm_nazca`, and `ibm_strasbourg`. Eagle r3 processor is a family of superconducting-based quantum processing units. They share a configuration of 127 qubits and a heavy-hex coupling graph.

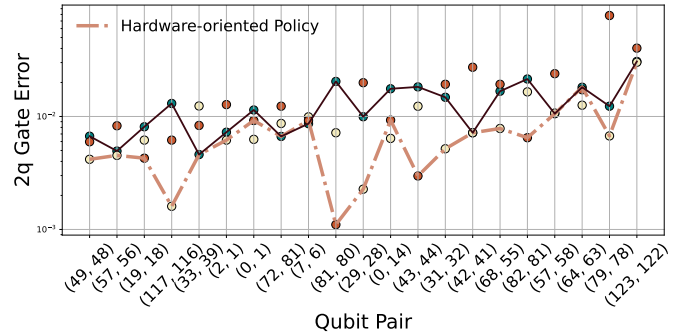
We implement Echoed CR pulses using symbolic functions in Qiskit. In contrast, multi-derivative DRAG pulses and Direct CR pulses are sent to the hardware as arrays of pulse amplitudes. Due to limitations in IBM quantum machines, we



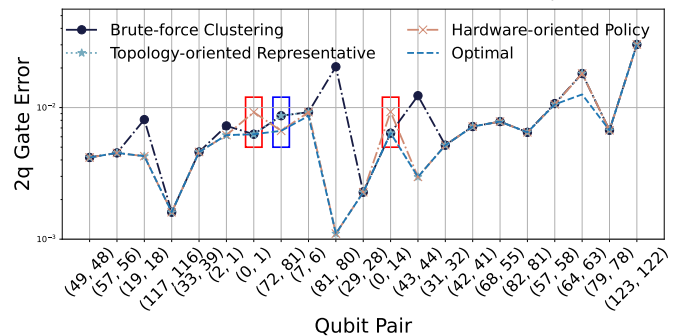
(a) Performance of Brute-force clustering with clustering size of 7. Echoed CR pulse is the default pulse waveform by IBM.



(b) Performance of Topology-oriented Representative.



(c) Performance of Hardware-oriented Policy.



(d) Horizontal comparison of the three profiling policies.

Fig. 12: Performance benchmarking of various waveform profiling policies on randomly selected qubit pairs.

split multi-derivative DRAG pulses into two parts to avoid overly complicated custom pulse shapes. We use SciPy [51] to process Hamiltonian tomography results and optimize pulse parameters. Before calibrating ECR gates, we focus on qubits whose single-qubit gate error rates were significantly higher than the device median. These calibrated single-qubit gates are later used in Hamiltonian tomography experiments. We initially set an error threshold of 0.015 MHz for all calibration experiments. If qubit pairs fail to meet this threshold after four calibration rounds, we increase the threshold to 0.3 MHz. Our results show that over 99% of qubit pairs could limit error terms to 0.3 MHz within four calibration rounds. To accurately measure the errors of ECR gates before and after calibration, we employ Interleaved Randomized Benchmarking (IRB) to assess waveform fidelity. Each IRB experiment uses sequence lengths of 1, 10, 20, 50, 100, 150, 250, and 400. We repeat each experiment five times for each pulse configuration to calculate the mean and standard deviation of the gate error. Therefore, the reported gate error represents the average error over the hours following calibration, which has included any drift in system parameters during that time.

B. Gate-level Benchmarking

In all policies for profiling optimal ECR gates’ waveforms, the primary goal is to achieve maximum fidelity across all qubit pairs. To evaluate whether this can be uniformly accomplished, we performed a comprehensive calibration of three waveforms on each qubit pair, beyond the standard calibration according to each policy.

Benchmarking results, displayed in Figure 12, include randomly selected qubit pairs with error terms restricted to 0.015 MHz and 0.03 MHz. For the 21 qubit pairs selected, the Brute-force Clustering method showed a significant increase in fidelity compared to the default echoed CR pulse provided by IBM. However, for about five qubit pairs, this method failed to select the waveform with the highest fidelity, as seen in Figure 12a. In contrast, the Topology-aware Representative method demonstrated higher accuracy in pulse profiling, with only two-qubit pairs not achieving the optimal waveform, as illustrated in Figure 12b. When comparing all three profiling policies in Figure 12d, the Hardware-oriented Policy achieved nearly the same fidelity as the Topology-aware Representative. For certain qubit pairs, it favored the Direct CR waveform due to its significantly reduced gate duration. For example, in the left blue box, the Hardware-oriented Policy selects the Direct CR waveform for qubit pair (0, 1) because qubit 1 has a T_2 time of only 82.99 μs , which is less than half the median value. In the right box, Direct CR is chosen for the qubit pair (0, 14) since it offers similar fidelity to the Multi-derivative DRAG waveform while maintaining a shorter duration. Meanwhile, as shown in the middle blue box, for qubit pair (72, 81) with frequency detuning outside the optimal range for the Multi-derivative DRAG waveform, the Hardware-oriented Policy automatically selects the echoed CR as the optimal pulse, resulting in a lower error rate.

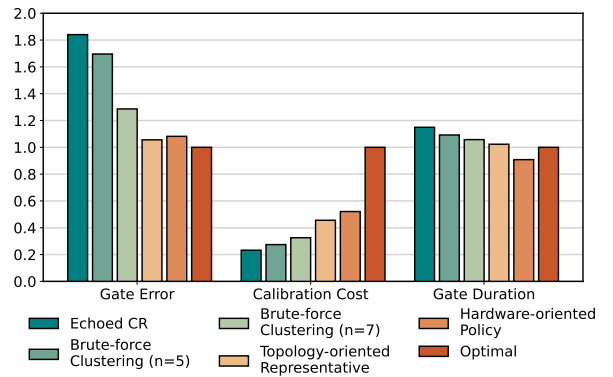


Fig. 13: The sum of the gate error rate, calibration cost, and gate duration for all qubit pairs based on various profiling policies. All metrics are normalized to the optimal.

To evaluate the performance of different policies, we considered three main metrics for each qubit pair: the sum of error rates, calibration cost, and gate durations. Figure 13 provides a detailed comparison of these metrics, with each normalized to its optimal value. The optimal calibration cost is calculated based on calibrating all three possible waveforms for every qubit pair. The Topology-oriented Representative policy achieves a total error rate close to the optimal scenario, effectively selecting the waveform with the highest fidelity for nearly all qubit pairs. Meanwhile, its total calibration cost is less than half of what it would be if all three waveforms were calibrated for each pair. The Hardware-oriented Policy also attains a similar total error rate compared to the optimal solution. Furthermore, it results in a significantly shorter total gate duration than other profiling policies, which could enable the execution of longer gate sequences within the decoherence limit.

Combining waveform selection for specific qubit pairs and the generalized results for the whole quantum machine, our fine-tuned protocol can achieve almost the optimal error rate on all qubit pairs while limiting the total gate duration. After applying the whole calibration process on the real quantum machine, the medium of the two-qubit gate error rate is reduced to 4.4×10^{-3} , representing a $1.84\times$ improvement compared to the default pulse configuration provided by IBM. For qubits with fabrication defects and shorter decoherence limits, the total pulse duration is reduced by a factor of 1.26. The proposed protocol could reduce the two-qubit gate error rate to the minimum at 1.3×10^{-3} . According to the real IBM quantum hardware results described in the [4], this error rate is already below the two-qubit gate error rate threshold (3×10^{-3}). It means that with our calibration method, the quantum error correction code has entered the region where errors are suppressed.

C. Calibration-level Benchmarking

Leveraging parallel graph traversal in the calibration process brings about a huge opportunity for acceleration. During

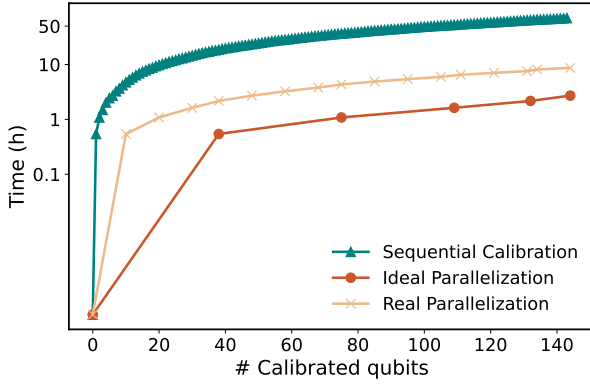


Fig. 14: Calibration time comparison among sequential calibration, ideal parallel calibration, and limited parallel calibration due to hardware limitations.

Quantum Device	Quantum Volume		Error Per Layered Gate	
	Default	Calibrated	Default	Calibrated
ibm_renselaer	128	256	3.08e-2	1.34e-2
ibm_nazca	128	256	2.94e-2	1.48e-2

TABLE I: Device-level benchmarking results for ibm_renselaer and ibm_nazca.

experiments on real quantum machines, it was observed that when the current calibration subgraph—representing all calibration tasks executed simultaneously—includes a large number of complex custom pulses defined by arrays, the parallel execution often results in errors. Therefore, calibration subgraphs that contain more than 20 edges are split into smaller graphs with no more than 10 edges each. When splitting the edges, edges that are scheduled for Direct CR calibration are separated from edges scheduled with other calibration methods. Therefore, the long calibration time of Direct CR does not interfere with the runtime of other subgraphs. The calibration subgraphs are then executed sequentially as previously mentioned. As shown in Figure 14, even limited by the hardware constraints, the parallel calibration could reduce the total runtime by a factor of 7.9. Given an ideal hardware, the improvement in runtime could be as large as 25 times.

D. Device-level Benchmarking

Quantum Volume. Quantum Volume is a single-number metric utilized to characterize the power of a quantum computer. The circuit used to measure Quantum Volume is composed of random unitaries involving d qubits and has a depth of d . Beginning with a small d , the Quantum Volume is measured with repetitive trails. Once the measurement outcome satisfies the fidelity requirement, the experiment proceeds with a larger d . The fidelity requirement is shown below

$$\frac{n_h - 2\sqrt{n_h(n_s - \frac{n_h}{n_c})}}{n_c n_s} > \frac{2}{3} \quad (4)$$

where n_h is the number of heavy outputs (outputs with probabilities higher than the median probability), n_c is the number of circuits created which is set to be 100, and n_s is the number of shots. Such a threshold checks if there is at least a 97% chance the heavy output probability is greater than $2/3$. Finally, until a square circuit with d depth cannot pass the fidelity requirement, the Quantum Volume is represented as 2^d .

Error Per Layered Gate (EPLG). As current quantum hardware scales to over 127 qubits, Quantum Volume is still a convincing holistic test of processor performance. However, it only contains d qubits with the highest fidelity. The layer fidelity fills the void as the protocol involves as many connected qubits as required. The layer fidelity is measured by splitting selected n qubits into M disjoint layers where each layer contains non-overlapping two-qubit gates and idle qubits. Simultaneous direct randomized benchmarking is conducted on the disjoint layer to measure the error of two-qubit gates and idle qubits. A process fidelity $F_i = \frac{1+(d^2-1)\alpha}{d^2}$ is obtained for each measured decay where $d = 2^n$, and α is the decay rate. The layer fidelity and EPLG is calculated as

$$LF = \prod_m \prod_j F_{j,m} \quad (5)$$

$$EPLG = 1 - LF^{1/n} \quad (6)$$

The device-level benchmarking results for ibm_renselaer and ibm_nazca are shown in Table I. For both machines, the Quantum Volume is enlarged from 128 to 256, indicating that the quantum processors are able to execute a square circuit with a width of 8 and a depth of 8. Meanwhile, the EPLG for ibm_renselaer is reduced by a factor of 2.3 while EPLG for ibm_nazca also achieves a reduction of 1.99 times, proving the overall improvement in two-qubit gate fidelity. From both local metric (QV) and global metric (EPLG), our optimal pulse profiling technique exhibits great potential in further elevating the performance of current quantum hardware.

E. Application-level Benchmarking

To evaluate the real-world effect brought about by the advanced optimal pulse profiling technique, several quantum programs from OpenQASMBench are adopted to examine the application-level performance. Through running programs on noise-free simulators, quantum computer with default pulse setup, and quantum computer with optimal pulse for each qubit pair, the error rate (E) and the fidelity (F) of each circuit are obtained as

$$E = \frac{1}{2} \sum_x |P_{\text{ideal}}(x) - P_{\text{real}}(x)| \quad (7)$$

$$F = \left(\sum_x \sqrt{P_{\text{ideal}}(x) \cdot P_{\text{real}}(x)} \right)^2 \quad (8)$$

where $P_{\text{ideal}}(x)$ represents the ideal probability of outcome x and $P_{\text{real}}(x)$ represents the actual probability of outcome x from real quantum hardware. As demonstrated in Table II, our

Benchmark	# Qubits	# ECR Gates	ECR Depth	Depth	Error Rate		Fidelity	
					Default	Calibrated	Default	Calibrated
adder_n4	4	16	10	41	0.13	0.10	0.87	0.90
adder_n10	10	146	136	503	0.56	0.49	0.44	0.51
dnn_n8	8	237	63	249	0.42	0.37	0.71	0.76
ising_n10	10	90	20	111	0.32	0.24	0.76	0.84
qpe_n9	9	97	86	339	0.15	0.07	0.94	0.98
cat_state_n22	22	21	21	66	0.39	0.36	0.61	0.64
ghz_state_n23	23	22	22	65	0.47	0.41	0.53	0.59
qram_n20	20	352	225	794	0.74	0.68	0.26	0.32

TABLE II: Application-level benchmarking results for `ibm_renselaer`.

optimal pulse profiling technique exhibits error rate reduction and fidelity increase in all benchmarks, with a maximum fidelity increase of 16%, proving its enormous potential in leveraging the hidden power of current quantum hardware.

VI. RELATED WORKS

Recent work on optimizing quantum circuits for higher Quantum Volume underscores the importance of gate speed in circuit performance [16]. Researchers have developed techniques to reduce two-qubit gate durations by incorporating pre- and post-single-qubit rotations into the compilation, effectively shortening the gate to its entangling component. Additionally, high-fidelity alternatives to traditional echo pulse sequences, like direct echo-free CX gates leveraging target rotary pulsing [44], have been proposed to eliminate extra single-qubit gates from the duration. These approaches demonstrate that a strategic balance between gate speed and fidelity can enhance overall circuit performance, however, this approach much more expensive than the ECR gate calibration in terms of the calibration cost.

And previous studies on CR gates have demonstrated significant advancements in mitigating control errors and achieving high-fidelity quantum operations. [24] inspired by the DRAG framework, introduces recursive corrections to mitigate single- and multi-photon transition errors, achieving improvement over standard calibration techniques, [8] leverages amplitude control of a microwave drive on one qubit at the resonance frequency of another to generate the desired interaction. However, those method overlooked the limitation on hardware inconsistencies and directly applies the same pulse envelope to all pairs of qubits.

VII. CONCLUSION

In this paper, we present a fine-grained calibration protocol that addresses both hardware variations and parallel execution needs in quantum computers. Our protocol combines three hardware-aware calibration policies with a graph-based method for parallel calibration. Experiments on quantum processors with up to 127 qubits demonstrate significant fidelity improvements while maintaining practical calibration overhead. This work advances hardware-aware calibration strategies and establishes a foundation for fault-tolerant quantum computing at scale.

VIII. ACKNOWLEDGEMENT

We acknowledge the usage of IBM Quantum Services for this work.

REFERENCES

- [1] Muhammad AbuGhanem. IBM quantum computers: Evolution, performance, and future directions. *arXiv preprint arXiv:2410.00916*, 2024.
- [2] Thomas Alexander, Naoki Kanazawa, Daniel J Egger, Lauren Capelluto, Christopher J Wood, Ali Javadi-Abhari, and David C McKay. Qiskit pulse: programming quantum computers through the cloud with pulses. *Quantum Science and Technology*, 5(4):044006, 2020.
- [3] Feng Bao, Hao Deng, Dawei Ding, Ran Gao, Xun Gao, Cupjin Huang, Xun Jiang, Hsiang-Sheng Ku, Zhisheng Li, Xizheng Ma, Xiaotong Ni, Jin Qin, Zhijun Song, Hantao Sun, Chengchun Tang, Tenghui Wang, Feng Wu, Tian Xia, Wenlong Yu, Fang Zhang, Gengyan Zhang, Xiaohang Zhang, Jingwei Zhou, Xing Zhu, Yaoyun Shi, Jianxin Chen, Hui-Hai Zhao, and Chunqing Deng. Fluxonium: an alternative qubit platform for high-fidelity operations. *Physical review letters*, 129(1):010502, 2022.
- [4] César Benito, Esperanza López, Borja Peropadre, and Alejandro Bermudez. Comparative study of quantum error correction strategies for the heavy-hexagonal lattice. *arXiv preprint arXiv:2402.02185*, 2024.
- [5] Colin D Bruzewicz, John Chiaverini, Robert McConnell, and Jeremy M Sage. Trapped-ion quantum computing: Progress and challenges. *Applied Physics Reviews*, 6(2), 2019.
- [6] Qi-Ming Chen, Herschel Rabitz, and Re-Bing Wu. Quantum optimal control without arbitrary waveform generators. *Physical Review Applied*, 20(6):064016, 2023.
- [7] John Chiaverini, Dietrich Leibfried, Tobias Schaetz, Murray D Barrett, RB Blakestad, Joseph Britton, Wayne M Itano, John D Jost, Emanuel Knill, Christopher Langer, Roe Ozeri, and David Wineland. Realization of quantum error correction. *Nature*, 432(7017):602–605, 2004.
- [8] Jerry M Chow, Antonio D Córcoles, Jay M Gambetta, Chad Rigetti, Blake R Johnson, John A Smolin, Jim R Rozen, George A Keefe, Mary B Rothwell, Mark B Ketchen, and M. Steffen. Simple all-microwave entangling gate for fixed-frequency superconducting qubits. *Physical review letters*, 107(8):080502, 2011.
- [9] D-Wave Systems. The advantage™ quantum computer, 2024. Accessed: 2024-11-20.
- [10] Poulami Das, Swamit Tannu, Siddharth Dangwal, and Moinuddin Qureshi. Adapt: Mitigating idling errors in qubits via adaptive dynamical decoupling. In *MICRO-54: 54th Annual IEEE/ACM International Symposium on Microarchitecture*, pages 950–962, 2021.
- [11] Jay M Gambetta, F Motzoi, ST Merkel, and Frank K Wilhelm. Analytic control methods for high-fidelity unitary operations in a weakly nonlinear oscillator. *Physical Review A—Atomic, Molecular, and Optical Physics*, 83(1):012308, 2011.
- [12] Pranav Gokhale, Ali Javadi-Abhari, Nathan Earnest, Yunong Shi, and Frederic T Chong. Optimized quantum compilation for near-term algorithms with openpulse. In *2020 53rd Annual IEEE/ACM International Symposium on Microarchitecture (MICRO)*, pages 186–200. IEEE, 2020.
- [13] M Fernando Gonzalez-Zalba. Silicon-based quantum computing: Scaling strategies. In *2022 IEEE Silicon Nanoelectronics Workshop (SNW)*, pages 1–2. IEEE, 2022.
- [14] W. Huang, C. H. Yang, K. W. Chan, T. Tanttu, B. Hensen, R. C. C. Leon, M. A. Fogarty, J. C. C. Hwang, F. E. Hudson, K. M. Itoh, A. Morello, A. Laucht, and A. S. Dzurak. Fidelity benchmarks for two-qubit gates in silicon. *Nature*, 569:532–536, 2019.
- [15] Yipeng Huang, Steven Holtzen, Todd Millstein, Guy Van den Broeck, and Margaret Martonosi. Logical abstractions for noisy variational quantum algorithm simulation. In *Proceedings of the 26th ACM international conference on architectural support for programming languages and operating systems*, pages 456–472, 2021.
- [16] Petar Jurcevic, Ali Javadi-Abhari, Lev S Bishop, Isaac Lauer, Daniela F Bogorin, Markus Brink, Lauren Capelluto, Oktay Gül, Toshihiko Itoko, Naoki Kanazawa, Abhinav Kandala, George A Keefe, Kevin Krulich, William Landers, Eric P Lewandowski, Douglas T McClure, Giacomo Nannicini, Adinath Narasgond, Hasan M Nayfeh, Emily Pritchett, Mary Beth Rothwell, Srikanth Srinivasan, Neereja Sundaresan, Cindy Wang, Ken X Wei, Christopher J Wood, Jeng-Bang Yau, Eric J Zhang, Oliver E Dial, Jerry M Chow, and Jay M Gambetta. Demonstration of quantum volume 64 on a superconducting quantum computing system. 6(2):025020, 2021.
- [17] Naoki Kanazawa, Daniel J Egger, Yael Ben-Haim, Helena Zhang, William E Shanks, Gadi Aleksandrowicz, and Christopher J Wood. Qiskit experiments: A python package to characterize and calibrate quantum computers. *Journal of Open Source Software*, 8(84):5329, 2023.
- [18] Paul V Klimov, Julian Kelly, John M Martinis, and Hartmut Neven. The snake optimizer for learning quantum processor control parameters. *arXiv preprint arXiv:2006.04594*, 2020.
- [19] Emanuel Knill, Dietrich Leibfried, Rolf Reichle, Joe Britton, R Brad Blakestad, John D Jost, Chris Langer, Roe Ozeri, Signe Seidelin, and David J Wineland. Randomized benchmarking of quantum gates. *Physical Review A—Atomic, Molecular, and Optical Physics*, 77(1):012307, 2008.
- [20] Jens Koch, Terri M. Yu, Jay Gambetta, A. A. Houck, D. I. Schuster, J. Majer, Alexandre Blais, M. H. Devoret, S. M. Girvin, and R. J. Schoelkopf. Charge-insensitive qubit design derived from the Cooper pair box. *Physical Review A*, 76(4):042319, October 2007.
- [21] Bálint Koczor, John JL Morton, and Simon C Benjamin. Probabilistic interpolation of quantum rotation angles. *Physical Review Letters*, 132(13):130602, 2024.
- [22] P. Krantz, M. Kjaergaard, F. Yan, T. P. Orlando, S. Gustavsson, and W. D. Oliver. A quantum engineer’s guide to superconducting qubits. *Applied Physics Reviews*, 6(2):021318, June 2019.
- [23] Aleksander Kubica and Michael Vasmer. Single-shot quantum error correction with the three-dimensional subsystem toric code. *Nature communications*, 13(1):6272, 2022.
- [24] Boxi Li, Tommaso Calarco, and Felix Motzoi. Experimental error suppression in Cross-Resonance gates via multi-derivative pulse shaping. *npj Quantum Information*, 10(1):1–10, July 2024.
- [25] Zhiding Liang, Jinglei Cheng, Hang Ren, Hanrui Wang, Fei Hua, Zhixin Song, Yongshan Ding, Frederic T Chong, Song Han, Xuehai Qian, and Yiyu Shi. Napa: intermediate-level variational native-pulse ansatz for variational quantum algorithms. *IEEE Transactions on Computer-Aided Design of Integrated Circuits and Systems*, 2024.
- [26] Ji Liu, Peiyi Li, and Huiyang Zhou. Not all swaps have the same cost: A case for optimization-aware qubit routing. In *2022 IEEE International Symposium on High-Performance Computer Architecture (HPCA)*, pages 709–725. IEEE, 2022.
- [27] Easwar Magesan and Jay M. Gambetta. Effective Hamiltonian models of the cross-resonance gate. *Physical Review A*, 101(5):052308, May 2020.
- [28] Easwar Magesan, Jay M Gambetta, Blake R Johnson, Colm A Ryan, Jerry M Chow, Seth T Merkel, Marcus P Da Silva, George A Keefe, Mary B Rothwell, Thomas A Ohki, Mark B. Ketchen, and M. Steffen. Efficient measurement of quantum gate error by interleaved randomized benchmarking. *Physical review letters*, 109(8):080505, 2012.
- [29] David C. McKay, Thomas Alexander, Luciano Bello, Michael J. Biercuk, Lev Bishop, Jiayin Chen, Jerry M. Chow, Antonio D. Córcoles, Daniel Egger, Stefan Filipp, Juan Gomez, Michael Hush, Ali Javadi-Abhari, Diego Moreda, Paul Nation, Brent Paulovicks, Erick Winston, Christopher J. Wood, James Wootton, and Jay M. Gambetta. Qiskit backend specifications for openqasm and openpulse experiments, 2018.
- [30] Masoud Mohseni, Ali T Rezakhani, and Daniel A Lidar. Quantum-process tomography: Resource analysis of different strategies. *Physical Review A—Atomic, Molecular, and Optical Physics*, 77(3):032322, 2008.
- [31] F. Motzoi and F. K. Wilhelm. Improving frequency selection of driven pulses using derivative-based transition suppression. *Physical Review A*, 88(6):062318, December 2013.
- [32] Felix Motzoi, Jay M Gambetta, Patrick Rebentrost, and Frank K Wilhelm. Simple pulses for elimination of leakage in weakly nonlinear qubits. *Physical review letters*, 103(11):110501, 2009.
- [33] Osama Moussa, Jonathan Baugh, Colm A Ryan, and Raymond Laflamme. Demonstration of sufficient control for two rounds of quantum error correction in a solid state ensemble quantum information processor. *Physical review letters*, 107(16):160501, 2011.
- [34] Paul Nation, Hanhee Paik, Andrew Cross, and Zaira Nazario. The IBM Quantum heavy hex lattice | IBM Quantum Computing Blog.
- [35] Kyungjoo Noh, Christopher Chamberland, and Fernando GSL Brandão. Low-overhead fault-tolerant quantum error correction with the surface-gkp code. *PRX Quantum*, 3(1):010315, 2022.
- [36] Tirthak Patel, Abhay Potharaju, Baolin Li, Rohan Basu Roy, and Devesh Tiwari. Experimental evaluation of nisq quantum computers: Error measurement, characterization, and implications. In *SC20: International conference for high performance computing, networking, storage and analysis*, pages 1–15. IEEE, 2020.
- [37] John Preskill. Quantum computing in the nisq era and beyond. *Quantum*, 2:79, 2018.

- [38] IBM Quantum. About calibration jobs, 2023. Accessed: 2024-11-19.
- [39] Gokul Subramanian Ravi, Kaitlin N Smith, Pranav Gokhale, Andrea Mari, Nathan Earnest, Ali Javadi-Abhari, and Frederic T Chong. Vaqem: A variational approach to quantum error mitigation. In *2022 IEEE International Symposium on High-Performance Computer Architecture (HPCA)*, pages 288–303. IEEE, 2022.
- [40] Philipp Schindler, Julio T Barreiro, Thomas Monz, Volckmar Nebendahl, Daniel Nigg, Michael Chwalla, Markus Hennrich, and Rainer Blatt. Experimental repetitive quantum error correction. *Science*, 332(6033):1059–1061, 2011.
- [41] Sarah Sheldon, Easwar Magesan, Jerry M. Chow, and Jay M. Gambetta. Procedure for systematically tuning up cross-talk in the cross-resonance gate. *Physical Review A*, 93(6):060302(R), June 2016.
- [42] V. V. Sivak, A. Eickbusch, B. Royer, S. Singh, I. Tsioutsios, S. Ganjam, A. Miano, B. L. Brock, A. Z. Ding, L. Frunzio, S. M. Girvin, R. J. Schoelkopf, and M. H. Devoret. Real-time quantum error correction beyond break-even. *Nature*, 616(7955):50–55, 2023.
- [43] Kaitlin N Smith, Gokul Subramanian Ravi, Jonathan M Baker, and Frederic T Chong. Scaling superconducting quantum computers with chiplet architectures. In *2022 55th IEEE/ACM International Symposium on Microarchitecture (MICRO)*, pages 1092–1109. IEEE, 2022.
- [44] Neereja Sundaresan, Isaac Lauer, Emily Pritchett, Easwar Magesan, Petar Jurcevic, and Jay M Gambetta. Reducing unitary and spectator errors in cross resonance with optimized rotary echoes. *PRX Quantum*, 1(2):020318, 2020.
- [45] Bochen Tan and Jason Cong. Optimal layout synthesis for quantum computing. In *Proceedings of the 39th International Conference on Computer-Aided Design*, pages 1–9, 2020.
- [46] Swamit Tannu, Poulami Das, Ramin Ayanzadeh, and Moinuddin Qureshi. Hammer: boosting fidelity of noisy quantum circuits by exploiting hamming behavior of erroneous outcomes. In *Proceedings of the 27th ACM International Conference on Architectural Support for Programming Languages and Operating Systems*, pages 529–540, 2022.
- [47] Swamit S Tannu, Zachary A Myers, Prashant J Nair, Douglas M Carnean, and Moinuddin K Qureshi. Taming the instruction bandwidth of quantum computers via hardware-managed error correction. In *Proceedings of the 50th Annual IEEE/ACM International Symposium on Microarchitecture*, pages 679–691, 2017.
- [48] Teague Tomesh and Margaret Martonosi. Quantum codesign. *IEEE Micro*, 41(5):33–40, 2021.
- [49] Lieven MK Vandersypen and Isaac L Chuang. Nmr techniques for quantum control and computation. *Reviews of modern physics*, 76(4):1037–1069, 2004.
- [50] M. Vinet, L. Hutin, B. Bertrand, S. Barraud, J.-M. Hartmann, Y.-J. Kim, V. Mazzocchi, A. Amisse, H. Bohuslavskiy, L. Bourdet, A. Crippa, X. Jehl, R. Maurand, Y.-M. Niquet, M. Sanquer, B. Venitucci, B. Jadot, E. Chanrion, P.-A. Mortemousque, C. Spence, M. Urdampilleta, S. De Franceschi, and T. Meunier. Towards scalable silicon quantum computing. In *2018 IEEE International Electron Devices Meeting (IEDM)*, pages 6–5. IEEE, 2018.
- [51] Pauli Virtanen, Ralf Gommers, Travis E. Oliphant, Matt Haberland, Tyler Reddy, David Cournapeau, Evgeni Burovski, Pearu Peterson, Warren Weckesser, Jonathan Bright, Stéfan J. Van Der Walt, Matthew Brett, Joshua Wilson, K. Jarrod Millman, Nikolay Mayorov, Andrew R. J. Nelson, Eric Jones, Robert Kern, Eric Larson, C J Carey, İlhan Polat, Yu Feng, Eric W. Moore, Jake VanderPlas, Denis Laxalde, Josef Perktold, Robert Cimrman, Ian Henriksen, E. A. Quintero, Charles R. Harris, Anne M. Archibald, Antônio H. Ribeiro, Fabian Pedregosa, Paul Van Mulbregt, SciPy 1.0 Contributors, Aditya Vijaykumar, Alessandro Pietro Bardelli, Alex Rothberg, Andreas Hilboll, Andreas Kloeckner, Anthony Scopatz, Antony Lee, Ariel Rokem, C. Nathan Woods, Chad Fulton, Charles Masson, Christian Häggström, Clark Fitzgerald, David A. Nicholson, David R. Hagen, Dmitrii V. Pasechnik, Emanuele Olivetti, Eric Martin, Eric Wieser, Fabrice Silva, Felix Lenders, Florian Wilhelm, G. Young, Gavin A. Price, Gert-Ludwig Ingold, Gregory E. Allen, Gregory R. Lee, Hervé Audren, Irvin Probst, Jörg P. Dietrich, Jacob Silterra, James T Webber, Janko Slavič, Joel Nothman, Johannes Buchner, Johannes Kulick, Johannes L. Schönberger, José Vinícius De Miranda Cardoso, Joscha Reimer, Joseph Harrington, Juan Luis Cano Rodríguez, Juan Nunez-Iglesias, Justin Kuczynski, Kevin Tritz, Martin Thoma, Matthew Newville, Matthias Kümmerer, Maximilian Bolingbroke, Michael Tartre, Mikhail Pak, Nathaniel J. Smith, Nikolai Nowaczyk, Nikolay Shebanov, Oleksandr Pavlyk, Per A. Brodtkorb, Perry Lee, Robert T. McGibbon, Roman Feldbauer, Sam Lewis, Sam Tygier, Scott Sievert, Sebastiano Vigna, Stefan Peterson, Surhud More, Tadeusz Pudlik, Takuya Oshima, Thomas J. Pingel, Thomas P. Robitaille, Thomas Spura, Thouis R. Jones, Tim Cera, Tim Leslie, Tiziano Zito, Tom Krauss, Utkarsh Upadhyay, Yaroslav O. Halchenko, and Yoshiki Vázquez-Baeza. Scipy 1.0: fundamental algorithms for scientific computing in python. *Nature methods*, 17(3):261–272, 2020.
- [52] Hanrui Wang, Zhiding Liang, Jiaqi Gu, Zirui Li, Yongshan Ding, Weiwei Jiang, Yiyu Shi, David Z Pan, Frederic T Chong, and Song Han. Torchquantum case study for robust quantum circuits. In *Proceedings of the 41st IEEE/ACM International Conference on Computer-Aided Design*, pages 1–9, 2022.
- [53] Chuanqi Xu, Ferhat Erata, and Jakub Szefer. Exploration of power side-channel vulnerabilities in quantum computer controllers. In *Proceedings of the 2023 ACM SIGSAC Conference on Computer and Communications Security*, pages 579–593, 2023.
- [54] Qian Xu, Guo Zheng, Yu-Xin Wang, Peter Zoller, Aashish A Clerk, and Liang Jiang. Autonomous quantum error correction and fault-tolerant quantum computation with squeezed cat qubits. *npj Quantum Information*, 9(1):78, 2023.
- [55] Yuan Xu, Ji Chu, Jiahao Yuan, Jiawei Qiu, Yuxuan Zhou, Libo Zhang, Xinsheng Tan, Jiang Yu, Song Liu, Jian Li, Fei Yan, and Dapeng Yu. High-fidelity, high-scalability two-qubit gate scheme for superconducting qubits. *Physical review letters*, 125(24):240503, 2020.